DISCLAIMER

Modeling Low-Platinum-Loading Effects in Fuel-Cell Catalyst Layers

Wonseok Yoon* and Adam Z. Weber**,[z]

Environmental Energy Technologies Division

Lawrence Berkeley National Laboratory

1 Cyclotron Rd., MS 70-108B, Berkeley, CA 94720, USA

The cathode catalyst layer within a proton-exchange-membrane fuel cell is the most complex and critical, yet least understood, layer within the cell. The exact method and equations for modeling this layer are still being revised and will be discussed in this paper, including a 0.8 reaction order, existence of Pt oxides, possible non-isopotential agglomerates, and the impact of a film resistance towards oxygen transport. While the former assumptions are relatively straightforward to understand and implement, the latter film resistance is shown to be critically important in explaining increased mass-transport limitations with low Pt-loading catalyst layers. Model results demonstrate agreement with experimental data that the increased oxygen flux and/or diffusion pathway through the film can substantially decrease performance. Also, some scale-up concepts from the agglomerate scale to the more macroscopic porous-electrode scale are discussed and the resulting optimization scenarios investigated.

* Electrochemical Society Student Member

** Electrochemical Society Active Member

[z] E-mail: azweber@lbl.gov

Introduction

The catalyst layer (CL) is a very complex chemical and geometric environment for electrochemical reactions in proton-exchange-membrane fuel cells (PEMFCs). It is composed of supported catalyst particles, ionomer, and gas pores. The reaction occurs at sites where various reacting species such as protons, electrons, and gases meet. Modeling the structure has been approached by various means[1], and a rigorous mathematical model of the CL is required to capture transport within the different phases, electrochemical reaction, and heat and water generation. Among previous models, one of the most accepted models is an agglomerate particle composed of the ionomer, gas voids, liquid water, and catalyst that is covered by a thin film of ionomer[2-28]. This idea is supported by various experimental observations such as scanning–electron- and transmission-electron-microscopy studies. In this model, oxygen is dissolved in the ionomer film surrounding the agglomerate, and the dissolved oxygen diffuses to the agglomerate where simultaneous transport and reaction occur. Typically, the agglomerate model is embedded (i.e., distributed uniformly across the CL) into a porous-electrode model to describe the CL fully[1]. _ENREF_29

Optimization of the CL for enhancing PEMFC performance is of great interest for researchers and industry. Parametric studies of CLs were accomplished by Yin[14] using an agglomerate model, with the model predicting the general polarization-curve trend as a function of parameters such as gas void fraction[7, 16] and ionomer[4, 5, 10, 29] and catalyst loadings[5, 10, 30-32] within the CL. Similarly, several optimization studies[16, 22, 30] using an agglomerate model were conducted to obtain optimum design parameters such as catalyst loading, CL thickness, and Pt/C ratio for best performance at a given potential. However, all the studies were based on several assumptions

and issues that are not correct validated or possibly correct including a lack of ionomer films and a first-order oxygen dependence for the oxygen reduction reaction (ORR).

For agglomerate particle radii of 1 micrometer or less, a back-of-the-envelope analysis shows that the particle will remain isothermal, even with the relatively thin, thermally resistive ionomer skin.[33] Deviations only occur when the thermal conductivity of the particles are extremely low and diffusion of reactant species high. Similarly, electron diffusion is not limiting and the particles can be assumed to be electronically isopotential. However, due to a structure in which there may be water or gas filling the agglomerates or due to possibly low conductivity of the ionomer within the CL, it is unclear as to whether the particles can be assumed to be ionically isopotential. In addition, the ORR within a fuel-cell CL has been shown to not be first order,[34] which is often assumed. Finally, the thin ionomer film around the agglomerate particles can limit the oxygen flux through the particles, and this should be evaluated.

One of the barriers against the commercialization of PEMFCs is the material cost, with the dominant one being that of Pt. Therefore, numerous research has focused on developing effective and economical ways to reduce the Pt loading without impacting overall performance (i.e., increase the mass activity). For traditional CLs, there are two main routes to lower the Pt loading. The first is to decrease the Pt/C ratio and the second is to make the CL thinner. Both cases though seem to have a limit in that unexplained resistances occur at very low loadings (< 0.1 mg/cm^2),[31, 32] that do not occur at higher loadings.[35] This effect has not been fully explained, and simulation is required to justify and explain the prevalent theories. It is thought that the resistance is due to changes in the kinetics due to the increased turnover rate required per Pt particle, resistance through the ionomer layer and/or agglomerate, or even contamination and poisoning.

In this paper, the kinetics and transport phenomena using an agglomerate model are systematically explored, including appropriate expressions for the overall rate expressions. Both agglomerate (1-D) and CL (1+1D) simulations are accomplished for the cathode CL. Below, we first discuss the modeling approach and examine both relevant kinetic and transport assumptions and effects. Next, some CL layer optimization with regards to agglomerate particles is explored as well as the impact of mass-transport limitations at low Pt loadings.

Theory

Governing equations

Here, we consider a single spherical particle of radius R_a with ionomer film having a thickness of δ_{film} at an arbitrary local point within the cathode CL as shown in Figure 1(a). Since no assumptions are made regarding proton and oxygen mass-transport, the two transport equations must be solved simultaneously,

$$\nabla \cdot (\kappa_m \nabla \Phi_2) + j_e = 0 \tag{1}$$

and

$$-\nabla \cdot (D_e \nabla C_{O_2}) = j_o \tag{2}$$

respectively,

where D_e is the effective diffusion coefficient of dissolved oxygen inside the particle, C_{O_2} is the oxygen concentration in the particle, j_o is oxygen molar consumption rate, κ_m is the ionomer phase conductivity, Φ_2 is the ionomer-phase potential, and j_e is the oxygen-reduction-reaction

rate. It should be noted that accurate estimations or measurements of the diffusion coefficient and ionomer conductivity inside the particle are almost impossible. In this study, reasonable values, some from literature and some from estimation, are used, and where appropriate they are varied to assess their impact.

The equations listed above are written in spherical coordinates (radial direction) and nondimensionalized. For example, the final equation form of the diffusion equation can be described as

$$\frac{1}{z^2(R_a+\delta_{film})}\frac{d}{dz}\left(z^2 D_e \frac{1}{(R_a+\delta_{film})}\frac{dC_{O_2}}{dz}\right)+j_{O_2}=0 \tag{3}$$

where $z = r / (R_a+\delta_{film})$ in the particle and

$$\frac{d}{dz}\left(z^2 D_{film} \frac{1}{(R_a+\delta_{film})}\frac{dC_{O_2}}{dz}\right)=0 \tag{4}$$

in the ionomer film.

The source terms for the two governing equations above are given as

$$j_{O_2}=-k_{c,n}C_{O_2}^n \tag{5}$$

and

$$j_e=-4Fk_{c,n}C_{O_2}^n \tag{6}$$

where

$$k_{c,n}=(1-\theta_{PtO})\frac{i_{ref}}{4FC_{ref,O_2}^n}\exp\left(-\frac{\alpha_c F}{RT}\eta_c\right) \tag{7}$$

$$i_{ref} = a_{pt} \cdot i_0 = \frac{L_{ca} A_{ca}}{\ell_{CL}} \cdot i_{0,s}^{*} \exp\left[\frac{-E_c^{rev}}{RT} \left(1 - \frac{T}{T^*} \right) \right] \tag{8}$$

where θ_{PtO} is the Pt-oxide coverage

The catalyst loading, L_{ca}, and electrochemical surface area, A_{ca}, are the critical parameters in determining PEMFC performance. To account for those effects, the exchange current density (A/cm^2_{Pt}) is based on active Pt area and the volumetric exchange current density is obtained by multiplying the catalyst specific current density by $L_{ca}A_{ca}/\ell_{CL}$. In this study, the catalyst loading and surface area obtained experimentally are used.[31]

For the boundary conditions, the oxygen concentration and overpotential are specified at the surface of the ionomer film and symmetry is used at the agglomerate center.

To determine the relative importance of transport phenomena and kinetics in an agglomerate, an effectiveness-factor approach is used.[36, 37] The effectiveness factor, *E*, can be described as a ratio of the actual reaction rate and a rate if the entire interior surface is exposed to the conditions outside of the particle.

$$E = \frac{4\pi R_a^2 \left(-D_e \left. \frac{dC_{O_2}}{dr} \right|_{r=R_a} \right)}{\frac{4}{3}\pi R_a^3 (-k_{s,n} C_{O_2,s}^n)} \tag{9}$$

The overall reaction rate is described by multiplication of the effectiveness factor by a rate constant and the surface-oxygen concentration. Most CL models using a particle model employ the effectiveness-factor approach for calculating the ORR.[11, 13, 16, 37-39] For a first-order reaction with no other transport limitations, an analytic expression for the effectiveness factor is obtained,[12, 14, 37]

$$E = \frac{3}{\Phi^2}\left(\Phi \coth \Phi - 1\right) \tag{10}$$

where Φ is the Thiele modulus

$$\Phi = R_a\sqrt{\frac{k_{a,n} C_{O_2,s}^{\beta-1}}{D_e}}\Phi = R_a\sqrt{\frac{k_{a,n} C_{O_2,s}^{\beta-1}}{D_e}}\Phi = R_a\sqrt{\frac{k_{a,n} C_{O_2,s}^{\beta-1}}{D_e}} \tag{11}$$

Kinetics

In this study, the overpotential is used as the variable of interest in the agglomerate particle.[15, 40] Since the solid-phase potential is assumed uniform within the particle and using a reference oxygen electrode, the cathode overpotential can be reduced to

$$\eta_c = \Phi_1 - \Phi_2 - U = \Phi_1 - \Phi_2 \tag{12}$$

and a potential gradient in the ohm's law for ionic current can be replaced by the gradient of local overpotential,

$$\nabla\eta_c = \nabla\Phi_1 - \nabla\Phi_2 = -\nabla\Phi_2 \tag{13}$$

where Φ_1 and Φ_2 are the solid- and ionomer-phase potentials, respectively, and U is the theoretical local equilibrium potential of a cathode with respect to the reference O_2 electrode.

The local cathode potential (local cell voltage) can be approximately calculated by[40]

$$\Phi_1 = E + \eta_c \tag{14}$$

$$E = E_O^0 + \frac{RT}{4F}\ln(Px_{O_2,in}) \tag{15}$$

The four electron ORR involves several intermediates oxides' absorption and desorption process which can make understanding the process more difficult. Platinum oxides form at the potential range of the ORR (0.6V ~ 1.0V) by water or gas-phase oxygen. These oxides can prohibit the ORR by blocking active Pt sites. Typically, a constant Tafel slope for the ORR kinetics around 60 to 70 mV/decade is assumed over the cathode potential range relevant to PEMFC operation. However, it has been suggested by experiments that this approach has to be modified to account for the potential-dependent oxide coverage as shown in equation (6).[41-43] Several forms of oxide can exist; OH coverage is considered in this study. The kinetic expression for the platinum oxidation and equilibrium coverage are given by

$$\frac{d\theta_{PtO}}{dt} = k_{PtO}\left((1-\theta_{PtO})\exp\left(\frac{\alpha_a' F}{RT}\eta_{PtO}\right) - \theta_{PtO}\exp\left(\frac{-\alpha_c' F}{RT}\eta_{PtO}\right)\right) \tag{16}$$

$$\theta_{PtO} = \frac{\exp\left[\frac{\alpha_a' F}{RT}\eta_{PtO}\right]}{\exp\left[\frac{\alpha_a' F}{RT}\eta_{PtO}\right] + \exp\left[\frac{-\alpha_c' F}{RT}\eta_{PtO}\right]} \tag{17}$$

$$\eta_{\mathrm{PtO}} = \Phi_{\mathrm{s}} - \Phi_{\mathrm{m}} - \mathrm{U}_{\mathrm{PtO}} \tag{18}$$

where k_{PtO}, η_{PtO}, and $\mathrm{U}_{\mathrm{PtO}}$ are the Pt-oxidation rate constant, overpotential, and equilibrium potential, respectively.

Figure 2 examines the impact of the oxide-coverage effect. A transfer coefficient, α_c, is set to 1 for the case when the Pt oxide is not taken into account and to 0.64 for the case when the Pt-oxide coverage is included in the ORR kinetic expression. This correction accounts for the

observed Tafel slope of around 120mV/decade when the oxide term is included[42]. As can be seen in Figure 2(a), the Pt-oxide coverage decreases as the cell potential decreases. This surface coverage effects the agglomerate current density at higher cell potentials (low overpotentials) due to the blockage of active sites by chemisorbed surface oxygen. The Pt-oxide term causes the Tafel slope to be potential dependent.[43] Figure 2(b) displays the impact of the Pt-oxide on a polarization curve using the half-cell model described below. The exchange current densities for the two cases are adjusted in a way that the current densities have the same value at a cell potential of 0.9 V, where most of the kinetic parameters have been measured.[34] At high cell potentials, the difference between the two cases is not obvious in this plot, but the cathode model for the case when the oxide coverage is considered produces higher current density at the same cell potential below 0.9 V and lower current density above 0.9 V as compared to the case of not considering Pt oxide. At low potentials, the curve becomes diffusion limited and Pt oxide does not have an effect.

Another key kinetic parameter is the oxygen reaction order. This value is widely assumed to be a value of 1, based on studies during the last couple of decades,[44-49] _ENREF_41 although other values have been obtained with Pt alloys.[50] However, these studies were done in liquid electrolytes and using rotating-disk-electrode methods. Recently, Gasteiger and coworkers[51-53] and Xu et al.,[54] conducted detailed experiments and analyses showing that under fuel-cell conditions and CL structures, the ORR oxygen reaction order is around 0.8 (referenced to an imaginary hydrogen reference electrode with its own extraneous phases) and not 1. This non-unity reaction order makes the diffusion equation become nonlinear and numerical solution is required to obtain the effectiveness factor. In general, as the reaction order increases, the effectiveness factor decreases for the same Thiele modulus.

Figure 3(a) explores the impact of the reaction order by showing simulated polarization curves with the two different reaction orders. It is clear that the performance curve with the reaction order of 0.8 is higher than the performance curve of the first-order reaction, since the oxygen partial pressure is always below its reference value. Non-unity reaction orders make the Thiele modulus dependent on the reactant concentration and thus the effectiveness factor varies with the reactant concentration. Figure 3(b) shows the variation of the effectiveness factor with respect to oxygen concentration at different overpotentials. At low overpotential, η_c = –0.38 V, the difference in the effectiveness factor is too small to differentiate one from the other, but at high overpotential, η_c = –0.68 V, the effectiveness factor for the reaction order of 0.8 clearly deviates from the value for the first-order reaction.

Figure 3 clearly demonstrates that the reaction order impacts PEMFC behavior. However, such a treatment requires numerical solvers since the Thiele modulus now depends on reactant concentration. One simple approach is to use the Thiele modulus with the reaction order (*n*) set to 0.8 (see Eq.12) with the effectiveness factor equation (11) derived for a first-order reaction. As shown in Figure 4, such an approach only results in minimal error, which is sufficient for most modeling purposes. It is therefore recommended that if the equipotential assumption is valid, one just uses the modified Thiele modulus above in the effectiveness factor expression. For the rest of this manuscript, a reaction order of 0.8 is used.

Transport

As noted above, assumptions of protonic isopotential and isothermal conditions are often made. As noted, the isothermal assumption is valid, and indeed our simulations confirm this unless the

heat conductivity is dramatically low and the oxygen diffusion coefficient inside the agglomerates is significantly high, thereby reacting near the core and keeping the heat within the particle. To examine the isopotential assumption, the proton conductivity is varied from 10^{-7} to 0.1 S/cm. Figure 5(a) shows the overpotential at the center of the particle. The overpotential remains at the same level of the surface overpotential when the conductivity varies from 0.1 to around 10^{-4} S/cm, but increases significantly when the conductivity decreases further down to 10^{-7} S/cm. This result indicates that the isopotential assumption is not valid if the proton conductivity is below 10^{-4} S/cm or so. Under these conditions, the effectiveness factor and current density are significantly impacted, as shown in Figure 5(b), especially at higher overpotentials (lower cell potentials). While for typical CLs, it is believed that the ionomer conductivity is sufficiently above the critical value,[55, 56] yet it remains to be measured unequivocally. In addition, one can envision cases, such as at very low humidities, that the conductivity is below this threshold value. Furthermore, recent molecular-dynamic studies[57-59] have shown that the inside of the agglomerate may not be filled with ionomer due to the chain-length size, thus suggesting that the conductivity within the agglomerate is very low or close to that of pure water (although there are ionic contaminants). While this issue needs some more experimental investigation, for most cases the assumption of uniform ionic potential is probably valid and will be used in this paper.

In general, the agglomerates are surrounded by an ionomer film that retards oxygen mass transport.[11, 12, 14] Since the exact properties and thickness of the film are unknown, a resistance approach (ratio of the film thickness and permeation coefficient) is used to represent the oxygen transport resistance of the film[60]

$$N_{O_2} = -D_{film}\nabla C_{O_2,diss} = -\frac{D_{film}H}{RT}\nabla P_{O_2,ext} = -\psi\,\nabla P_{O_2,ext} \tag{19}$$

$$R_{O_2,film} = \frac{\delta_{film}}{\psi} \tag{20}$$

where D_{film} is the oxygen diffusion coefficient in the ionomer film, $C_{O_2,diss}$ is the dissolved oxygen concentration, $R_{O_2,film}$ is the transport resistance of oxygen through ionomer film, H is the dimensionless Henry's constant, and $P_{O_2,ext}$ is the partial pressure of the dissolved oxygen outside of the film. In addition, one can imagine a liquid-water film around particles as well. In terms of diffusion, a liquid-water film has a similar effect as an ionomer film, and thus adding a liquid-water film is equivalent to changing the film transport resistance (adjusting for the respective transport properties and thicknesses of the films) in the above treatment.

To evaluate the importance of the film, one can compare the external (including film) and internal (no film limitations) effectiveness factors, where both are defined in a similar manner as actual reaction rate over the rate if outside conditions are present everywhere (see equation 10). Figure 6 shows the overall and internal effectiveness factors with respect to film thickness. As can be seen, there is a steep drop of the overall effectiveness factor showing how a film quickly can limit oxygen concentration and performance. For reference, assuming bulk-Nafion properties, a resistance of 0.01 m^2 s bar/mol is equivalent to a film thickness of 11 nm; however, it is believed that the thin ionomer film is more glassy and thus lower gas transport than for the bulk membrane.

Half-cell model

The agglomerate model developed above is coupled with a macroscopic porous CL model to examine the effects of model parameters for the particle models on PEMFC performance. This means that the coupled physical phenomena in different length scales need to be solved together. In this study, this coupling is realized by using a 1+1D, non-dimensional approach for particle models as shown in Figure 1(b). The z-direction denotes the dimensionless length across the CL and the y direction indicates the radial direction of each particle located in a position z. For the particle model in the 1+1D space, all the fluxes such as oxygen diffusion flux and current flow are defined in the y direction only, and the fluxes through the z-direction are enforced to be negligible.

This 1+1D particle model can provide reaction source terms that are required in cell-level models, such as oxygen consumption rate per volume of the CL and reaction current per volume of the CL[40]. The general equations can be expressed by

$$J_{O_2} = -\frac{(1-\varphi_c)}{4\pi(R_a+\delta_{film})^3/3}\cdot(4\pi R_a^2)\frac{D_e}{(R_a+\delta_{film})}\frac{\partial C_{O_2}}{\partial y}\bigg|_{y=\frac{R_a}{R_a+\delta_{film}}} \tag{21}$$

$$= -\frac{(1-\varphi_c)}{4\pi(R_a+\delta_{film})^3/3}\cdot[4\pi(R_a+\delta_{film})^2]\frac{D_{film}}{(R_a+\delta_{film})}\frac{\partial C_{O_2}}{\partial y}\bigg|_{y=1} \tag{22}$$

$$J_e = -\frac{(1-\varphi_c)}{4\pi(R_a+\delta_{film})^3/3}\cdot[4\pi(R_a+\delta_{film})^3]\int_0^{\frac{R_a}{R_a+\delta_{film}}} 4Fk_{c,n}C_{O_2}^n y^2 dy \tag{23}$$

where φ_c is gas phase porosity in the CL, J_o is the oxygen consumption rate, and J_e is the reaction current per unit volume in the CL, calculated from the 1+1D agglomerate particle models.

Gas-phase transport in the gas-diffusion layer (GDL) and CL is described by multicomponent diffusion, Stefan-Maxwell equation and liquid water is not considered in this model (the gases are assumed to be humidified but below saturated).

$$\frac{1}{\ell}\nabla x_i = \sum_{j \neq i} \frac{x_i N_j - x_j N_i}{c_T D_{i,j}^{eff}} \tag{24}$$

$$D_{ij}^{eff} = \varphi^{1.5} D_{ij}^{o} \tag{25}$$

$$D_{ij}^{o}(T,P) = D_{ij}^{o}(T_1,P_1) \times \frac{P_1}{P} \times \left(\frac{T}{T_1}\right)^{1.8} \tag{26}$$

In above equations, D_{ij}^{eff} is the effective binary interaction parameter between species i and j described by Bruggeman relation and ℓ is the length of GDL or CL, and c_T is the total concentration of all of the gas species.

For the cathode, oxygen, water vapor, and nitrogen are considered and mass-balance equations for the oxygen and water vapor in the porous region result in the following expressions (assuming that nitrogen flux equals zero since it does not participate in the reactions)

$$\frac{1}{\ell}\nabla \cdot (c_T v_G x_i) = -\frac{1}{\ell}\nabla \cdot N_i + S_i \quad \text{in the GDL and CL} \tag{27}$$

where S is the corresponding source term, and $v_G = -\frac{k_G}{\mu_G}\frac{1}{\ell}\nabla p_G$. To keep the analysis simple, viscosity, μ_G, and permeability, k_G, are assumed constant. Source terms for oxygen and water vapor in GDL and CL can be expressed as follows:

$$S_{O_2} = 0, \quad S_{H_2O(v)} = 0 \quad \text{in GDL} \tag{28}$$

$$S_{O_2} = J_{O_2}, \quad S_{H_2O(v)} = -\frac{1}{2} J_e (1 + 2n_d)/F \qquad \text{in the CL} \tag{29}$$

Electron transport and proton transport are described by Ohm's law,

$$\frac{1}{\ell}\nabla \cdot (\sigma_s^{eff} \frac{1}{\ell}\nabla \Phi_s) - S = 0 \quad \text{in the GDL and CL} \tag{30}$$

$$\frac{1}{\ell}\nabla \cdot (\kappa_m^{eff} \frac{1}{\ell}\nabla \Phi_m) + S = 0 \quad \text{in the CL} \tag{31}$$

$$S = 0 \quad \text{in the GDL, and} \quad S = J_e \quad \text{in the CL} \tag{32}$$

Boundary conditions for all of the physics are tabulated in Table I. It should be note that 1+1D agglomerate particle models require the oxygen concentration and overpotential profile across the CL as boundary conditions (0<= z <=1, y=1, in Figure 1(b)). All other exterior boundary conditions are insulation except for internal boundary between ionomer film and particle, which is continuity.

For oxygen concentration, it is assumed that the oxygen concentration outside of the particle is in equilibrium with the oxygen concentration on the particle surface described by Henry's law,[40]

$$C_{O_2}\Big|_{y=1} = c_T H x_{O_2} \tag{33}$$

where x_{O_2} is the mole fraction of the oxygen in the CL.

Results and discussions

The agglomerate and half-cell models described above are employed to examine the PEMFC performance and to investigate how the agglomerate size can impact performance. In addition, the impact of the oxygen film resistance on for low Pt-loading electrode is of particular interest. For all of the analyses below, the full 1+1D model described above with an oxygen transport resistance of $R_{O_2,film}$ = 0.01 m^2 s bar/mol is used. The agglomerate particle size is assumed to be 0.1 μm and the other model parameters used for the simulation are listed in Table II.

Catalyst-Layer Optimization

To understand the reaction-rate distribution, Figure 7 shows the effectiveness factor and rate profiles at various cell potentials. The reaction rate is uniform at high potentials and becomes much more nonuniform at lower ones. For the set of properties used in these simulations, the oxygen transport in the CL is somewhat limiting, thereby causing a higher rate near the GDL boundary, although at high current densities ohmic losses begin to also change the shape of the distribution.

It is of interest to examine how the particle-size distribution can impact PEMFC performance. To do this, first, a set of optimization studies is performed for the case when the film thickness varies proportionally with the particle radius. The ratio of the film thickness and particle radius is fixed to a value of 0.1, which corresponds to the ratio of 10nm film thickness and 100 nm particle radius. The first case being examined is that when the particle radius varies linearly from 10nm to 190nm from GDL side to membrane side and the second case is opposite; the average of the particle size is 0.1 um for all cases. Figure 8(a) shows the polarization curves of the two cases and baseline, uniform case. Interestingly, the particle distribution from large to small size (GDL to membrane) generates small performance increases in the high-current-density region than the

other cases. The comparison of the average effectiveness factor (averaged over the CL thickness) for the three cases which mirrors and causes the current-density response reveals that the usage of catalyst particles for the third case can be maximized at the given distribution pattern. Since the oxygen concentration at the boundary between GDL and CL is the highest than any other locations across the CL, and the concentration at the boundary between the CL and membrane is the lowest due to the reaction occurring across the CL, large particles at the GDL/CL and small particles at the CL/membrane can maximize utilization of the catalyst particles. However, when the film thickness is fixed to a constant value (which may be more realistic of the actual microstructure), both gradient cases show lower performance compared to the uniform baseline, which can be seen in Figure 8(b). This is because the film has a larger and counter effect for the small particles and thus limits the performance increase even though there is a gain from the large particles. Overall, these simulations show that optimization of particle size within the CL does not seem to provide a great benefit, especially when one considers that under operation the virgin distribution undoubtedly evolves.

Low Pt-loading electrodes

As mentioned, very low Pt-loading electrodes are recently being fabricated and explored to reduce PEMFC cost. However, experimental studies show that both reducing the Pt/C ratio or the CL thickness results in additional mass-transfer limitations. It is thought that this may be due to the increased oxygen flux to the Pt surface as shown in Figure 9.[32] Here, we attempt to explore the above two cases through modeling. Reducing the CL thickness can be easily implemented by changing the thickness parameter in the dimensionless governing equations; however, there is

another parameter that needs to be adjusted as well: the Pt loading. Typically, the Pt loading is calculated by measuring the total weight of Pt (mg_{Pt}) deposited in the CL followed by dividing it by the geometric electrode area (cm^2_{geo}). Therefore, Pt loading decreases as the CL thickness decreases due to the reduction of the total amount of Pt deposited in the CL. However, to see the impact of decreasing Pt loading by changing CL thickness, one is required to keep the volumetric Pt loading (L_{ca}/ℓ_{CL} , mg_{Pt}/cm^3) constant for all CL thicknesses. Since the same composition of catalyst ink is used for fabrication of CLs with different thicknesses, this should be a correct approach to account for the CL-thickness effect. The electrochemical surface area (ECSA) also needs to be measured for different Pt loadings and taken into account in the modeling. For this study, roughness-factor data (cm^2_{pt}/cm^2_{geo}) obtained from experiments was used for the relationship between Pt loading (L_{ca}) and ECSA (A_{ca}).[31]

Polarization curves for three different CL thickness, 15, 10, and 5 μm are plotted in Figure 10. Comparison of the polarization curves with and without ionomer film reveals that at low current density, performance of the PEMFC with the thin CL is lower than that with the thick CL due to the decreased Pt loading. However, at high current density, the performance with the thinner CL increases for both cases with and without ionomer film. Specifically, when the CL thickness is 5 μm and there is 10nm film, the rate of performance increase is limited due to the film, but still shows a slightly higher performance than 10 μm thick. The reason for the higher performance at high-current-density region can be explained by the increase of the average oxygen concentration in the thinner CL.

The question may arise from these results because our models completely ignore the liquid water build-up in the CL at high current density region. However, the effect of the liquid water on transport with respect to the thickness of CLs requires the relationships between capillary pressure and liquid-water saturation for different thickness of CLs, something that is not available currently in literature (although we are measuring it). Also, our studies are based on PEMFCs operating at lower humidity levels.

The results above seem to be counter to those of Nonoyama et al.,[32] who witnessed worse performance in thinner CLs and a subsequent increase in a mass-transport-related resistance. Furthermore, they also mention that they observed no significant oxygen mass-transport limitations in their CLs. To examine this contradiction, the diffusion coefficient of oxygen in the CL is increased and the simulations rerun at two different cell potentials (0.8V and 0.5V), and the normalized value of the current density are plotted as a function of CL thickness and four different film transport resistance; the results are shown in Figure 11. For the cell potential of 0.5 V with the fast diffusion coefficients (Figure 11(b)) , the comparison of the film and no-film curves show that the PEMFC performance with the ionomer film decreases with decreasing the CL thickness, indicating that the oxygen transport loss in these CL structures outweighs the loss of electrochemical reaction volume. In addition, the film causes a significant change in the limiting current. This implies that for thin CLs with low Pt loadings, the ionomer film covering the agglomerate can become limiting and a significant barrier to mass transport, in accordance with Figure 9. However, at low current density (0.8V), the PEMFC performance decreases greatly with decreasing the CL thickness with normal diffusion coefficients as plotted in Figure 11(c), implying that the performance is not limited by the oxygen transport; the normalized current density with the fast diffusion coefficients almost overlaps the plot with the normal

diffusion coefficients. Both cases show that the film adds mass-transport resistance which increases steeply as the CL thickness decreases. The curves also demonstrate that at higher oxygen resistances, the bend in the curve occurs at thicker CLs (higher Pt loadings).

The other method of lowering the Pt content is by diluting it by decreasing the Pt/C ratio for the same CL thickness. This has been seen experimentally to result in much lower performance, as shown in the data obtained by Makharia and coworkers.[31] To further investigate this phenomenon, the five different Pt loadings are simulated and compared to the data. The experiments were conducted at 90^{o}C, 50% O_2, and fully humidified, and the data was mass-transport and IR corrected. Therefore, all the initial conditions for the simulation are fit to match with the experimental conditions and the CL model is solved only to correct the GDL mass-transport loss. A film thickness of 15 nm is assumed and the model is fit to the 0.4 mg_{Pt}/cm^2 Pt-loading polarization data by adjusting other model parameters such as the exchange current density and film resistance. Next, only the Pt loading and ionomer film thickness (which modified the resistance, see equation 20) are modified to fit the rest of the data. The results are shown in Figure 12(a). For the three loading cases of 0.4, 0.2, and 0.1 mg_{Pt}/cm^2, changing the loading parameter is enough to fit the model to the experimental data. However, for the low-loading cases, the film thickness needs to be doubled to fit accurately the polarization curves. This implies that the oxygen transport resistance becomes significant if the Pt loading is below a certain value. The cause could be similar to that above, i.e., a longer diffusional path or higher flux through the ionomer film (see Figure 9). As a point of discussion, if one plots the cell potential plot versus catalyst specific activity, Figure 12(b), then one can see that the various polarization curves collapse. This collapse signifies that although the Pt sites at lower loadings are doing more work (i.e., increased turnover rate) they are not showing any deviations due to

this kinetic effect and thus are not turnover rate limited. However, the increased rate per Pt signifies that there is an increased oxygen flux to that site to maintain the reaction rate, and this increased flux must be supported by oxygen transport from other locations.

In reality, oxygen diffusion through agglomerate particles occurs in 3-D. In a 1-D analysis, the diffusion path is assumed to be in the radial direction only. However, when the Pt loading becomes very low, which means that the reaction site in the agglomerate particles is distributed sporadically, oxygen must diffuse along the other directions to reach the active site; this additional diffusion path needs to be accounted for.

The results in Figure 12 seem to suggest that for a 1-D model, some kind of effective film thickness is required due to transport limitations in the other dimensions. To explore this in more detail, 2-D simulations of a particle surface are conducted. In this study, a quarter of an agglomerate particle is modeled with a 10 nm thick ionomer film and a 10 nm reaction volume (although this is not critical to the analysis); the modeling domain is shown in Figure 13(a). A total of twelve equivalent reaction zones were created and distributed uniformly along the circumference of the particle. To mimic the different loading cases, the number of activated (reaction can occur) and deactivated (no reaction) reaction zones is controlled while keeping the distance between adjacent reaction zones as uniform as possible. The case numbers and corresponding zones are given in Table III. Twelve different cases were created and solved with all the same conditions. For boundary conditions, a current density of 0.025 A/cm^2 is applied to the exterior surface of the film for all cases as well as constant oxygen concentration and temperature. As an example, the resulting concentration of oxygen and reactant flux for case #1 and case #12 are shown in Figure 13(b) and (c), respectively. From the simulation results, the average concentration of oxygen around the reaction-zone boundaries is determined.

Figure 14 shows the normalized (to case #1) oxygen concentration for all the different cases. The normalized concentrations are around unity for most of the cases until the last few, where it decreases dramatically. A more resistive or thicker film causes a steeper drop as expected. Thus, there seems to be a significant mass-transport limitation at lower loadings, which agrees with the experimental results. To make a more rigorous comparison, an effective ionomer thickness can be calculated. Since Fickian diffusion is assumed through the ionomer film, the change in the oxygen concentration is directly related to the same increase in ionomer-film thickness. Thus, from Figure 14, for case #12, the effective thickness is slightly more than half when the active zones or loading is 1/12. This value compares very favorably with the required doubling of the ionomer-film thickness required to fit the data in Figure 12 when the loading went from 0.4 to 0.03 mg/cm^2 (a decrease of 1/13). Similarly, the trends of Figure 12 are also reproduced and represented in Figure 14. Overall, the ionomer film causes significant and unexpected mass-transport limitations at very low Pt loadings no matter the cause. However, decreasing the loading by changing the Pt/C ratio rather than the CL thickness seems to enhance the effect. It should be noted that one would not expect these resistances to exist for agglomerates and CLs that do not contain ionomer films (e.g., extended surface Pt structures), although water films could have a similar effect.

Conclusions

In this paper, a proton-exchange-membrane-fuel-cell cathode catalyst layer is modeled with a focus on explaining mass-transport limitations with low Pt-loaded catalyst layers. The modeling includes the observed effects of Pt oxide, ionomer film, and a 0.8 reaction order with respect to oxygen. In addition, the impact of assuming protonic isopotential conditions was explored with

the determination that this assumption is probably valid under most conditions. Simulations of cathode catalyst layers demonstrated that there is not a great benefit to optimizing the agglomerate particle-size distribution. The cathode CL model and a 1+1D particle-surface model clearly showed that the ionomer film that covers the agglomerate results in a mass-transport limitation that increases drastically at low Pt loadings. The cause of this was shown to be due to the higher oxygen fluxes through the ionomer film and longer diffusion pathways. While changing Pt loading by decreasing the catalyst-layer thickness or the Pt/C ratio both demonstrate these effects, they are more pronounced in the Pt/C ratio case. Although not shown, transient simulations exhibit the same conclusions and trends.

Acknowledgements

The authors would like to thank Drs. Nobuaki Nonoyama and Rohit Makharia for their input, data sharing, and discussion. Funding for this project was provided by the Assistant Secretary for Energy Efficiency and Renewable Energy, Office of Hydrogen, Fuel Cell, and Infrastructure Technologies, of the U. S. Department of Energy under contract number DE-AC02-05CH11231 and CRADA agreement LB08003874 between LBNL and Toyota Motor Company.

List of Symbols

b Tafel slope, V

C_{O2} oxygen concentration in an agglomerate particle, mol/cm^3

c_T total concentration of gas phase, mol/cm^3

D_e effective diffusion coefficient of dissolved oxygen inside the particle, cm^2/s

D_{film} effective diffusion coefficient of oxygen in ionomer film, cm^2/s

D_{ij}^{eff} effective binary diffusion coefficient in GDL and CL, cm^2/s

E equilibrium potential of fuel cell reaction with respect to hydrogen reference electrode, V

E_c^{rev} activation energy of the ORR at the reversible cell potential, kJ/mol

F Faraday's constant, 96487 C/equiv

R_a Particle radius, μm

$i_{0,s}^*$ catalyst specific exchange current density, A/cm_{pt}^2

j_{O_2} molar rate of reaction in an agglomerate particle, mol/cm^3 s

j_e oxygen reduction reaction current in an agglomerate particle, A/cm^3

J_{o_2} oxygen consumption rate in CL, mol/cm^3 s

J_e reaction current per unit volume of the CL, A/cm^3

$k_{c,n}$ rate constant of oxygen reduction reaction, nth order reaction, varies

k_{pto} rate constant for Pt oxidation, 1/s

k_G effective permeability of the gas phase, cm^2

ℓ_k length of GDL or CL, μm

N_i superficial flux density of species i, $mol/cm^2 \cdot s$

n_d osmotic drag coefficient

L_{ca} Pt loading, mg_{pt}/cm^2

A_{ca} electrochemical surface area, cm^2_{pt}/mg_{Pt}

H Henry's constant

P Total gas phase pressure, pa

r radial coordinate

R universal gas constant, 8.3143 J/mol K

S source term in mass balance equations

T absolute temperature, K

T^* reference temperature, K

U equilibrium potential, V

v_G mass averaged velocity,

$x_{O_2,in}$ inlet Oxygen mole fraction

x mole fraction of oxygen

y nondimensional length in radial direction for 2-D agglomerate model

z nondimensional length in radial direction for 1-D agglomerate model and nondimensional length for 1-D cathode model

Greek

α_a anodic transfer coefficient

α_c cathodic transfer coefficient

θ_{PtO} Platinum oxide coverage

δ_{film} thickness of ionomer film, nm

ε_i porosity phase i

σ_s conductivity of the electronically conducting phase, S/cm

κ_m conductivity of the ionically conducting phase, S/cm

Φ_2 ,Φ_m ionomer phase potential, V

Φ_1, Φ_s solid phase potential, V

μ_G viscosity of the gas phase, pa s

η_c cathode overpotential, V

η_{PtO} overpotential for platinum oxidation, V

η_{eff} effectiveness factor

ω water vapor mole fraction

ψ gas permeation coefficient through ionomer film, mol/s m bar

Φ Thiele modulus

Subscripts

1 solid, electronically conducting phase

2 membrane, ionically conducting phase

a anodic

c cathodic

G gas phase

s solid phase, agglomerate particle surface

m ionomer phase

o standard value

e effective property

diss dissolved

ext external

Superscripts

eff effective property

ref value taken at a reference condition

References

1. A. Z. Weber and J. Newman, *Chem.Rev.*, **104**, 4679 (2004).
2. J. Liu and M. Eikerling, *Electrochimica Acta*, **53**, 4435 (2008).
3. Q. Wang, D. Song, T. Navessin, S. Holdcroft and Z. Liu, *Electrochimica Acta*, **50**, 727 (2004).
4. Q. Wang, M. Eikerling, D. Song, Z. Liu, T. Navessin, Z. Xie and S. Holdcroft, *J. of the Electrochem.Soc.*, **151**, A950 (2004).
5. M. Srinivasarao, D. Bhattacharyya, R. Rengaswamy and S. Narasimhan, *Chem. Eng. Res Des*, **doi:10.1016/j.cherd.2010.04.020** (2010).
6. M. Srinivasarao, D. Bhattacharyya, R. Rengaswamy and S. Narasimhan, *International Journal of Hydrogen Energy*, **35**, 6356 (2010).
7. D. Song, Q. Wang, Z. Liu, T. Navessin and S. Holdcroft, *Electrochimica Acta*, **50**, 731 (2004).
8. R. Roshandel and B. Farhanieh, *International Journal of Hydrogen Energy*, **32**, 4424 (2007).
9. S. Kamarajugadda and S. Mazumder, *J. of Power Sources*, **183**, 629 (2008).
10. N. Khajeh-Hosseini-Dalasm, M. J. Kermani, D. Ghadiri Moghaddam and J. M. Stockie, *International Journal of Hydrogen Energy*, **35**, 2417 (2010).
11. F. Jaouen, G. Lindbergh and G. Sundholm, *J. of the Electrochem.Soc.*, **149**, A437 (2002).
12. W. Sun, B. A. Peppley and K. Karan, *Electrochimica Acta*, **50**, 3359 (2005).
13. K. Broka and P. Ekdunge, *J. of Applied Electrochem.*, **27**, 281 (1997).
14. K. M. Yin, *J. of the Electrochem.Soc.*, **152**, A583 (2005).

15. R. M. Rao and R. Rengaswamy, *J. of Power Sources*, **158**, 110 (2006).
16. M. Secanell, K. Karan, A. Suleman and N. Djilali, *Electrochimica Acta*, **52**, 6318 (2007).
17. D. Gerteisen, A. Hakenjos and J. O. Schumacher, *J. of Power Sources*, **173**, 346 (2007).
18. P. Berg, A. Novruzi and K. Promislow, *Chemical Engineering Science*, **61**, 4316 (2006).
19. S.-M. Chang and H.-S. Chu, *J. of Power Sources*, **172**, 790 (2007).
20. M. Chisaka and H. Daiguji, *Electrochemistry Communications*, **8**, 1304 (2006).
21. D. Harvey, J. G. Pharoah and K. Karan, *J. of Power Sources*, **179**, 209 (2008).
22. P. Jain, L. T. Biegler and M. S. Jhon, *Electrochem. and Solid-State Letters*, **11**, B193 (2008).
23. C.-Y. Jung, C.-H. Park, Y.-M. Lee, W.-J. Kim and S.-C. Yi, *International Journal of Hydrogen Energy*, **35**, 8433 (2010).
24. S. Obut and E. Alper, *J. of Power Sources*, **196**, 1920 (2011).
25. K. M. Yin, *J Appl Electrochem*, **37**, 971 (2007).
26. M. Eikerling, *J. of the Electrochem.Soc.*, **153**, E58 (2006).
27. Z. Xia, Q. Wang, M. Eikerling and Z. Liu, *Can. J. Chem.*, **86**, 657 (2008).
28. Q. Wang, M. Eikerling, D. Song and Z. Liu, *J. of Electroanalytical Chemistry*, **573**, 61 (2004).
29. E. Antolini, L. Giorgi, A. Pozio and E. Passalacqua, *J. of Power Sources*, **77**, 136 (1999).
30. D. Song, Q. Wang, Z. Liu, M. Eikerling, Z. Xie, T. Navessin and S. Holdcroft, *Electrochimica Acta*, **50**, 3347 (2005).
31. R. Makharia, Challenges Associated with High Current Density Performance of Low Pt-Loading Cathodes in PEM Fuel Cells, in *8th International Fuel Cell Science, Engineeriung & Technology Conference*, ASME, Brooklyn, NY (2010).

32. N. Nonoyama, S. Okazaki, A. Z. Weber, Y. Ikogi and T. Yoshida, *J Electrochem Soc*, **158**, B416 (2011).
33. A. A. Kulikovsky, *J. of Electroanalytical Chemistry*, **652**, 66 (2011).
34. K. C. Neyerlin, W. Gu, J. Jorne and H. A. Gasteiger, *J. of the Electrochem.Soc.*, **153**, A1955 (2006).
35. H. A. Gasteiger, J. E. Panels and S. G. Yan, *J. Power Sources*, **127**, 162 (2004).
36. H. S. Fogler, *Elements of Chemical Reaction Engineering*, Prentice Hall Inc. (1992).
37. F. Gloaguen and R. Durand, *J. of Applied Electrochem.*, **27**, 1029 (1997).
38. F. Jaouen and G. Lindbergh, *J. of the Electrochem.Soc.*, **150**, A1699 (2003).
39. P. Jain, L. T. Biegler and M. S. Jhon, *J. of the Electrochem.Soc.*, **157**, B1222 (2010).
40. Q. Guo and R. E. White, *J. of the Electrochem.Soc.*, **151**, E133 (2004).
41. Y. Liu, M. Mathias and J. Zhang, *Electrochem. and Solid-State Letters*, **12**, B1 (2010).
42. J. X. Wang, J. Zhang and R. R. Adzic, *J.Phys.Chem.A*, **111**, 12702 (2007).
43. S. Gottesfeld, *ECS Transactions*, **6**, 51 (2008).
44. A. Parthasarathy, S. Srinivasan, A. J. Appleby and C. R. Martin, *J. Electrochem. Soc.*, **139**, 2856 (1992).
45. A. Parthasarathy, S. Srinivasan, A. J. Appleby and C. R. Martin, *J. Electronanal. Chem.*, **339**, 101 (1992).
46. D. B. Sepa and M. V. Vojnovic, *Electrochimica Acta*, **26**, 781 (1981).
47. D. B. Sepa, M. V. Vojnovic and L. M. Vracar, *Electrochimica Acta*, **32**, 129 (1987).
48. A. J. Appleby, *J. of the Electrochem.Soc.*, **117**, 328 (1970).
49. U. A. Paulus, T. J. Schmidt, H. A. Gasteiger and R. J. Behm, *J. of Electroanalytical Chemistry*, **495**, 134 (2001).

50. S. Mukerjee and S. Srinivasan, *J. Electroanal. Chem*, **357**, 201 (1993).

51. K. C. Neyerlin, W. Gu, J. Jorne, A. Clark and H. A. Gasteiger, *J. Electrochem. Soc.*, **154**, B279 (2007).

52. K. C. Neyerlin, W. B. Gu, J. Jorne and H. A. Gasteiger, *J. Electrochem. Soc.*, **153**, A1955 (2006).

53. K. C. Neyerlin, H. A. Gasteiger, C. K. Mittelsteadt, J. Jorne and W. B. Gu, *J. Electrochem. Soc.*, **152**, A1073 (2005).

54. H. Xu, Y. Song, H. R. Kunz and J. M. Fenton, *J. of the Electrochem.Soc.*, **152**, A1828 (2005).

55. Y. Sone, P. Ekdunge and D. Simonsson, *J. of the Electrochem.Soc.*, **143**, 1254 (1996).

56. J. Fang, X. Guo, S. Harada, W. Tatsuya, K. Tanaka, H. Kita and K.-i. Okamoto, *Macromolecules*, **35**, pp 9022 (2002).

57. T. Mashio, K. Malek, M. Eikerling, A. Ohma, H. Kanesaka and K. Shinohara, *J.Phys.Chem. C*, **114**, 13739 (2010).

58. T. Mashio, K. Malek, M. Eikerling, K. Shinohara and A. Ohma, in *ISE*, Nice, France (2010).

59. M. E. Hannach, in *ISE*, Nice, France (2010).

60. A. Z. Weber and J. Newman, *J. of the Electrochem.Soc.*, **151**, A311 (2004).

61. R. Makharia, in *8th International Fuel Cell Science*, Brooklyn, NY (2010).

Caption

Figure 1(a) Illustration of an agglomerate particle and 1-D computational domain of the particle used for this study and (b) illustration of dimensionless 1-D cathode model (PEM is not modeled)

Figure 2(a) Platinum oxide coverage in terms of cell potential and (b) performance curve of the cathode model with and without the PtO coverage.

Figure 3 Simulated (a) polarization curves and (b) effectiveness-factor variation with respect to oxygen concentration when the reaction order is 1 and 0.8.

Figure 4 Comparison of the effectiveness factor from the analytic solution with Thiele modulus corrected for n=0.8, and the numerically calculated effectiveness factor for n=0.8.

Figure 5 (a) Overpotential profile at center of the agglomerate particle with respect to proton conductivity and (b) the effectiveness factor and agglomerate current density at the surface of the particle (The surface overpotential is -0.68V)

Figure 6 The overall effectiveness factor and internal effectiveness factor with respect to ionomer film thickness (The surface overpotential is -0.68V)

Figure 7 (a) Overall effectiveness-factor profile and (b) oxygen molar-consumption rate at different cell potentials across the catalyst layer.(0 is GDL/CL and 1 is CL/MEM boundary.)

Figure 8 (a) Comparison of polarization curves for the cases of three different particle distributions when the film thickness varies proportionally and (b) when the film oxygen resistance is constant, $R_{O_2,film} = \delta_{film}/\Psi$ **= 0.01 m^2 s bar/mol.**

Figure 9 Schematic image of oxygen transport through the ionomer film for (a) normal CL structure and two low Pt-loading cases, (b) thinner CL, and (c) low Pt/C ratio. Figure adopted from reference 32.

Figure 10 Polarization curves without (a) and with (b) ionomer film for three different CL thicknesses, $R_{O_2,film} = \delta_{film}/\Psi =$ 0.01 m^2 s bar/mol.

Figure 11 Current density at 0.5V with different film thicknesses with respect to the CL thickness (a) normal diffusion coefficients, (b) fast diffusion coefficients in the CLs, and (c) current density at 0.8V with different film thicknesses with respect to the CL thickness and normal diffusion coefficients

Figure 12 (a) Comparison of polarization curves with different Pt loadings between experimental data [61] (points) and model results and (b) simulated cell potential as a function of catalyst specific activity.

Figure 13 (a) Computational domain of two dimensional simplified agglomerate particle model, (b) a simulation result showing oxygen concentration and flux for case #1, and (c) at case #12. (Current density of 0.025A/cm^2 at the surface is given)

Figure 14 (a) Normalized oxygen concentration around the reaction zones and (b) concentration drop at case #9, 10, 11, and 12 with respect to agglomerate current density and two different film resistances.

Table I Boundary conditions for 1D cathode model

Table II Model parameters for baseline simulation of agglomerate particle models and CL models

Table III Case number and distribution of activated and deactivated reaction zones for each case (O = active reaction zone, X = deactivated reaction zone)

Table I Boundary conditions for 1D cathode model

Variable	**Ch/GDL**	**GDL/CL**	**CL/Mem**
x_{O_2}	$x_{O_2}\ given$	$N_o\big\vert_{z=1,GDL} = N_o\big\vert_{z=0,CL}$	$N_o\big\vert_{z=1,CL} = 0$
ω	$\omega\ given$	$N_\omega\big\vert_{z=1,GDL} = N_\omega\big\vert_{z=0,CL}$	$N_\omega\big\vert_{z=1,CL} = 0$
P_G	$P_G\ given$	$N\big\vert_{z=1,GDL} = N\big\vert_{z=0,CL}$	$N\big\vert_{z=1,CL} = 0$
Φ_s	$\Phi_s\ given$	$\frac{1}{\ell_{GDL}}\sigma_{GDL}^{eff}\nabla\Phi_s\Big\vert_{z=1,GDL} = \frac{1}{\ell_{CL}}\sigma_{CL}^{eff}\nabla\Phi_s\Big\vert_{z=0,CL}$	$\nabla\Phi_{s,z=1,CL} = 0$
Φ_m	*N/A*	$\nabla\Phi_{m,z=0,CL} = 0$	$\Phi_m = 0$

Table II Model parameters for baseline simulation of agglomerate particle models and CL models

Parameter		Value	
Temperature	T	80	°C
Total gas pressure	P	1.1	bar
Particle radius	R_a	0.1	μm
Oxygen inlet mole fraction	$x_{O_2,in}$	0.1472	
Water vapor inlet mole fraction	ω_{in}	0.22	
Inlet relative humidity		50	%
Surface oxygen concentration for the particle model	C_s	$1e^{-7}$	mol/cm^3
Cathodic transfer coefficient (with Pt oxide)	α_c	0.64	
Cathodic transfer coefficient (w/o Pt oxide)	α_c	1	
Equilibrium potential	E_O^o	1.2	V
ORR exchange current density (with Pt oxide)	$i_{0,s}^*$	0.00147	A/cm^2_{Pt}
ORR exchange current density (w/o Pt oxide)	$i_{0,s}^*$	1.5×10^{-6}	A/cm^2_{Pt}
CL porosity	φ_c	0.1	
GDL porosity	φ_{GDL}	0.4	
CL thickness	ℓ_{CL}	15	μm
GDL thickness	ℓ_{GDL}	300	μm
Pt loading	L_{ca}	0.2	mg_{Pt}/cm^2
Electrochemical surface area	A_{ca}	43.257	m^2_{Pt}/g_{Pt}
Activation energy of the ORR at the reversible cell potential[34]	E_c^{rev}	67	kJ/mol
Reference temperature[34]	T^*	353	K
Osmotic drag coefficient	n_d	1	
ionomer conductivity in a film and particle	κ_m	0.01	S/cm
Oxygen diffusion coefficient in a ionomer film[12]	D_{film}	8.45×10^{-6}	cm^2/s
Effective oxygen diffusion coefficient in the particle	D_e	8.45×10^{-5}	cm^2/s
Equilibrium potential for Pt oxide formation	U_{PtO}	0.76	V
Anodic transfer coefficient for Pt oxide formation	α_a'	0.4	
Cathodic transfer coefficient for Pt oxide formation	α_c'	0.4	
Oxygen/water diffusion coefficient[40] (T_1=308K, P_1 = 1atm)	D_{O_2,H_2O}	0.282	cm^2/s
Oxygen/Nitrogen diffusion coefficient[40] (T_1=316K, P_1 = 1atm)	D_{O_2,N_2}	0.230	cm^2/s
Nitrogen/water diffusion coefficient[40] T_1 =298K, P_1 = 1atm)	D_{N_2,H_2O}	0.293	cm^2/s
Henry's constant[40]	H	0.0277	
Effective permeability of gas phase	k_G	1×10^{-9}	cm^2
Viscosity of gas phase	μ_G	2.1×10^{-5}	Pa s

Table III Case number and distribution of activated and deactivated reaction zones for each case (O = active reaction zone, X = deactivated reaction zone)

Case number	Segments from top to bottom											
1	O	O	O	O	O	×	O	O	O	O	O	O
2	O	O	×	O	O	O	O	O	×	O	O	O
3	O	O	×	O	O	O	×	O	O	×	O	O
4	O	O	×	O	O	×	O	O	×	O	O	×
5	O	×	O	O	×	O	×	O	×	O	×	O
6	×	O	×	O	O	×	O	×	O	×	O	×
7	×	O	×	×	O	×	O	×	O	×	O	×
8	×	×	O	×	×	O	×	×	O	×	×	O
9	×	×	O	×	×	×	O	×	×	O	×	×
10	×	×	O	×	×	×	×	×	O	×	×	×
11	×	×	×	×	×	O	×	×	×	×	×	×
12	O	×	×	×	×	×	×	×	×	×	×	×

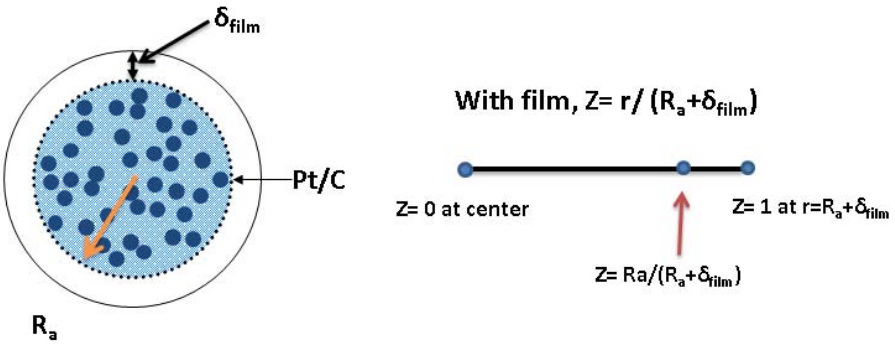

(a)

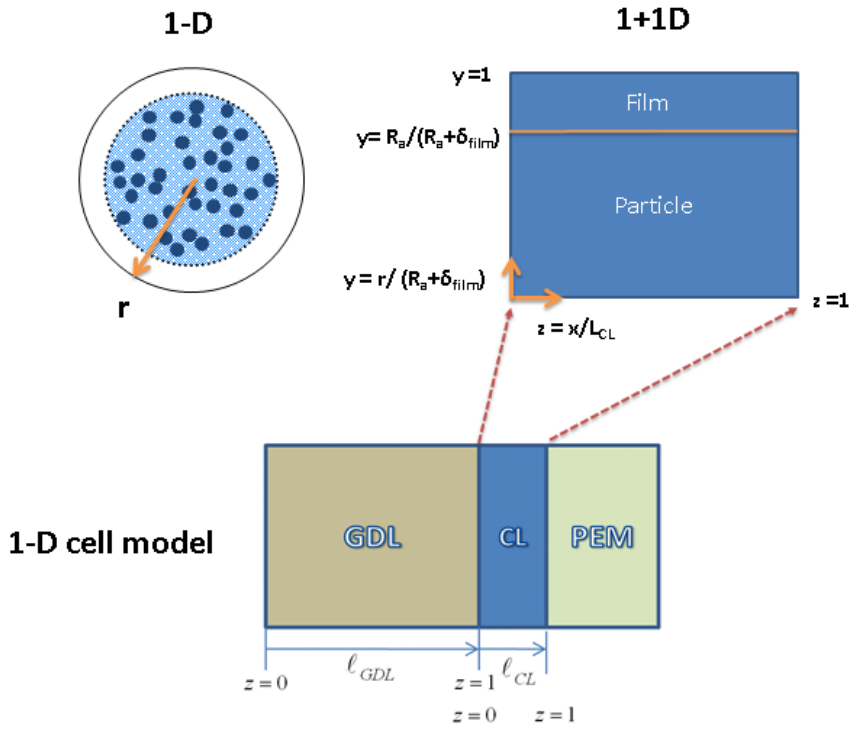

(b)

Figure 1(a) Illustration of an agglomerate particle and 1-D computational domain of the particle used for this study and (b) illustration of dimensionless 1-D cathode model (PEM is not modeled)

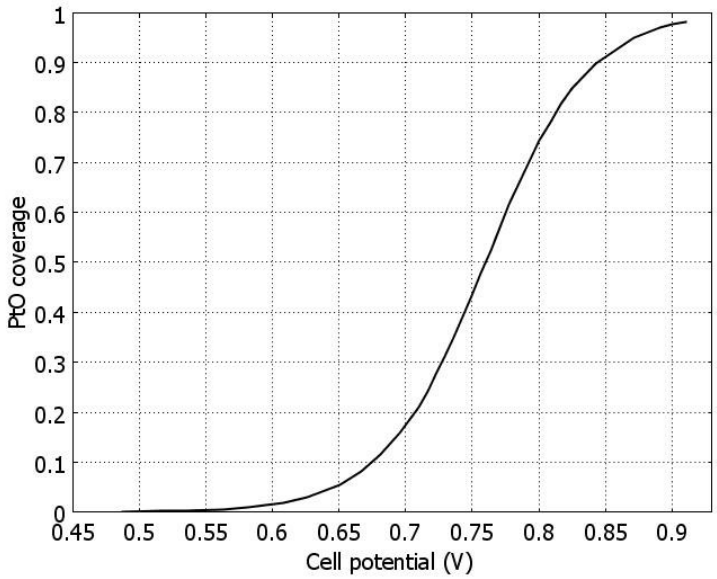

(a)

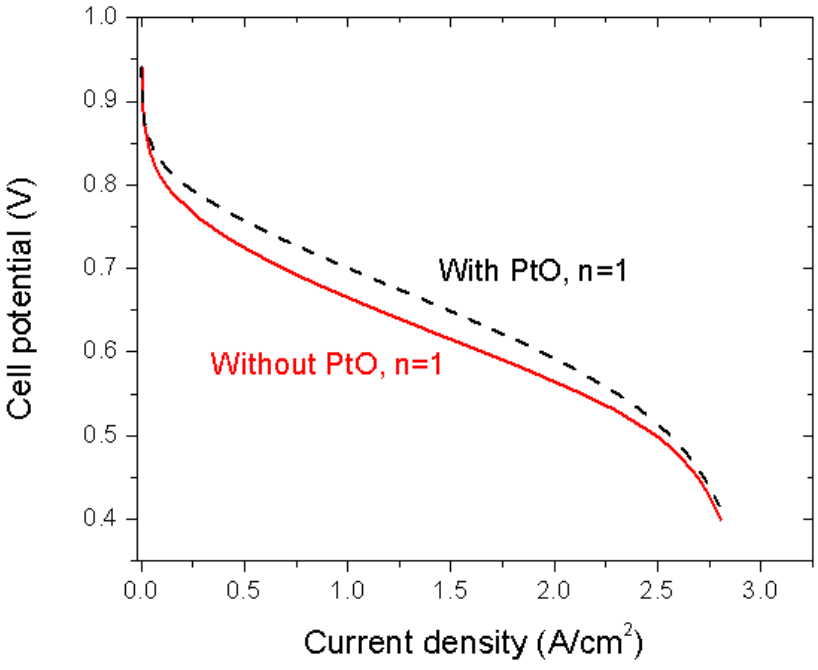

(b)

Figure 2(a) Platinum oxide coverage in terms of cell potential and (b) performance curve of the cathode model with and without the PtO coverage.

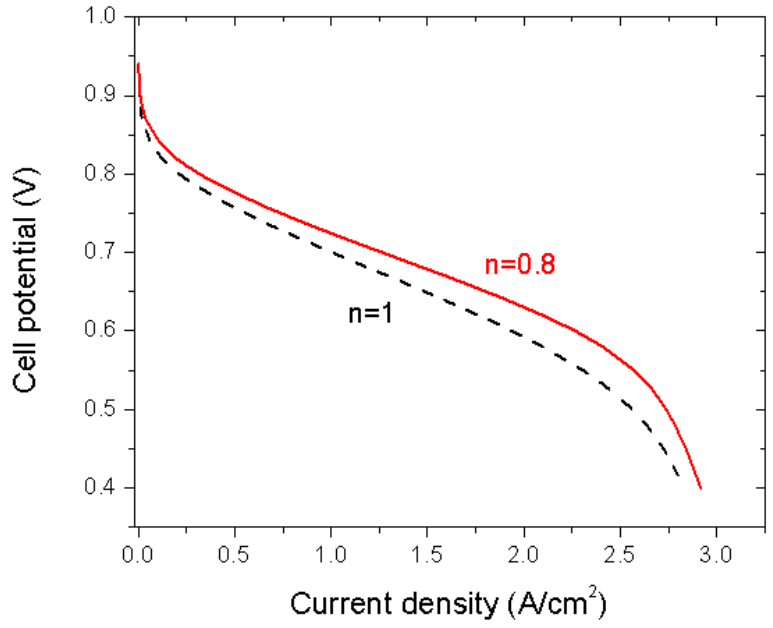

(a)

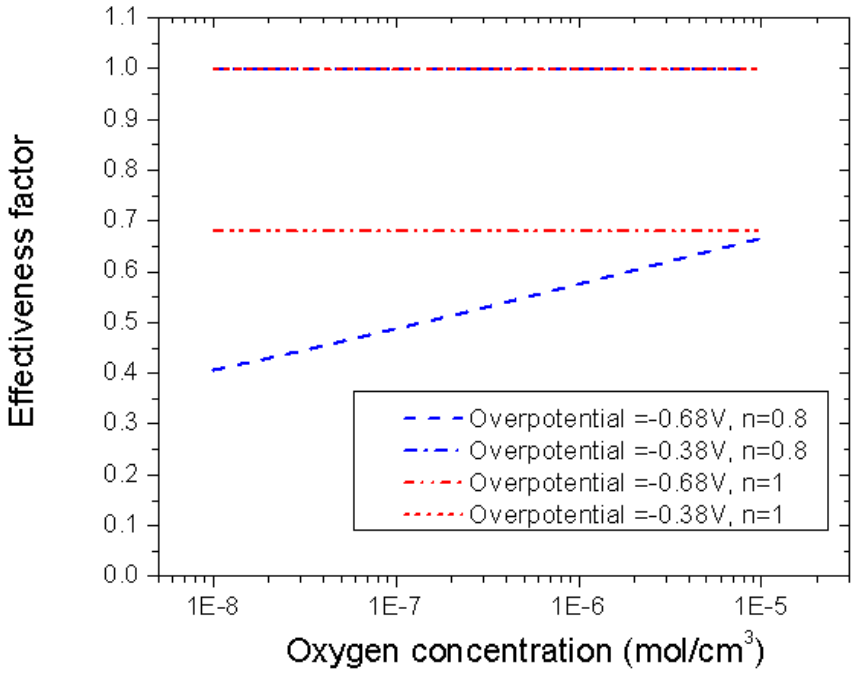

(b)

Figure 3 Simulated (a) polarization curves and (b) effectiveness-factor variation with respect to oxygen concentration when the reaction order is 1 and 0.8.

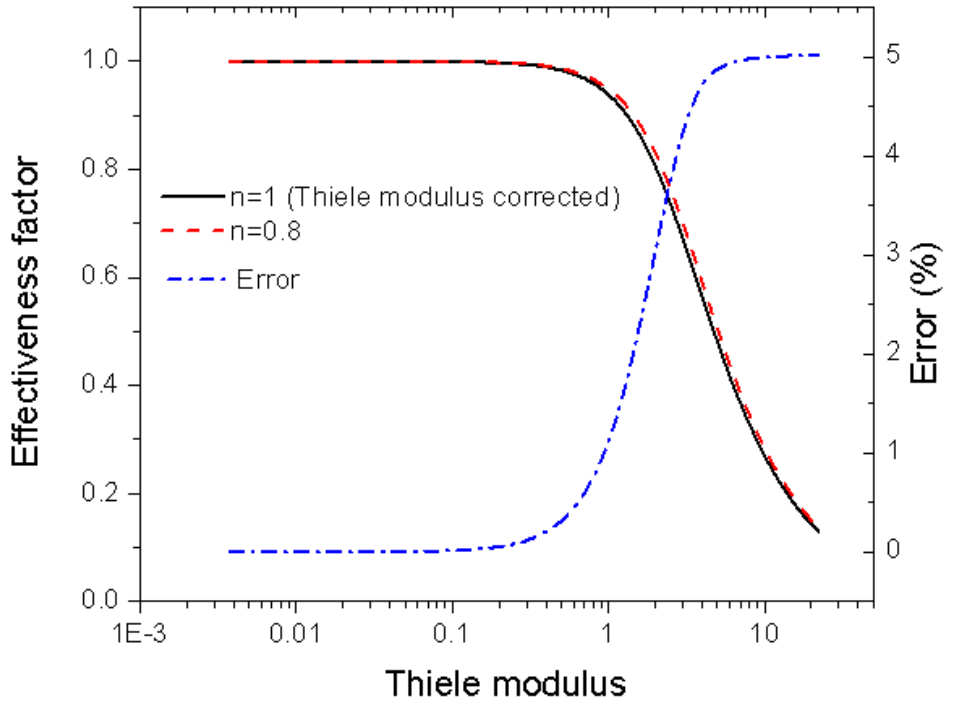

Figure 4 Comparison of the effectiveness factor from the analytic solution with Thiele modulus corrected for n=0.8, and the numerically calculated effectiveness factor for n=0.8.

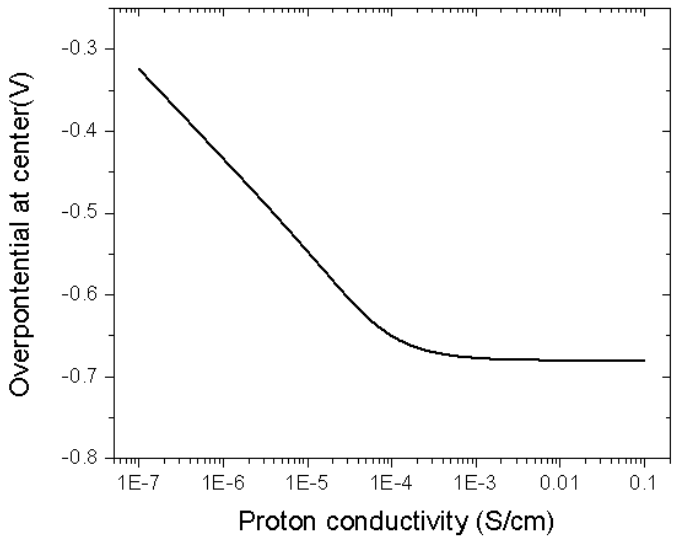

(a)

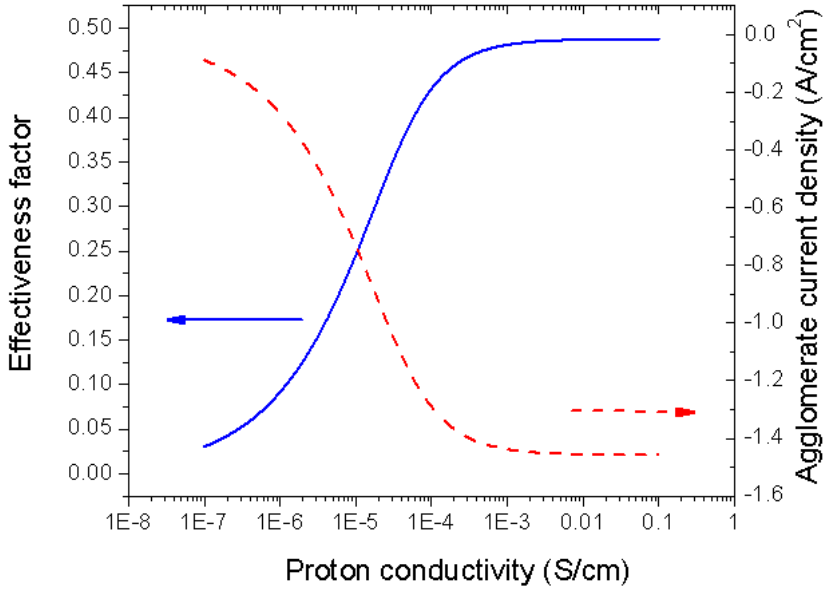

(b)

Figure 5 (a) Overpotential profile at center of the agglomerate particle with respect to proton conductivity and (b) the effectiveness factor and agglomerate current density at the surface of the particle (The surface overpotential is -0.68V)

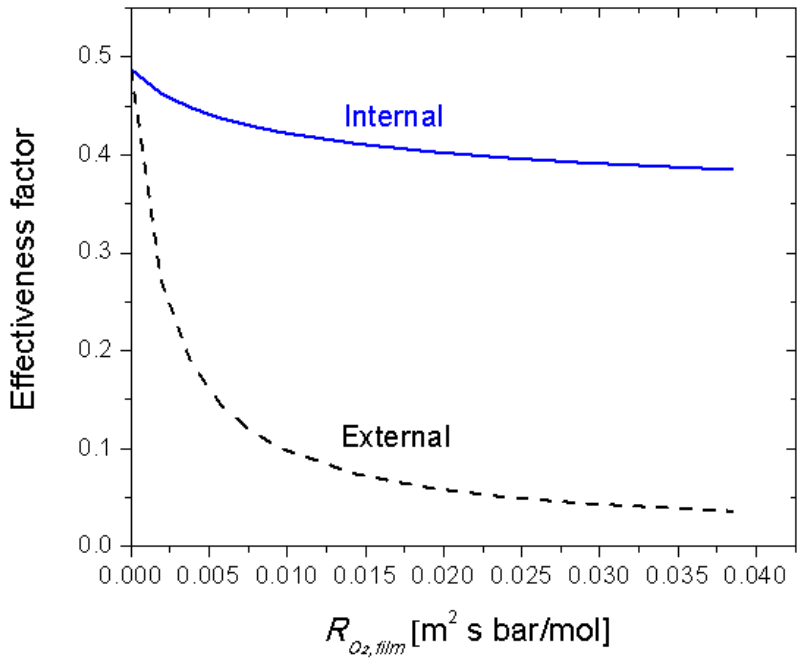

Figure 6 The overall effectiveness factor and internal effectiveness factor with respect to ionomer film thickness (The surface overpotential is -0.68V)

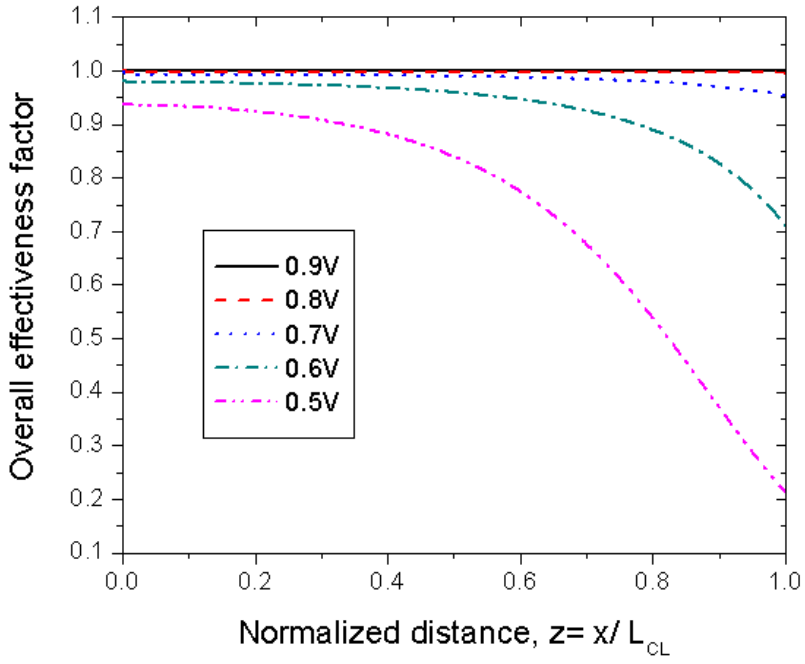

(a)

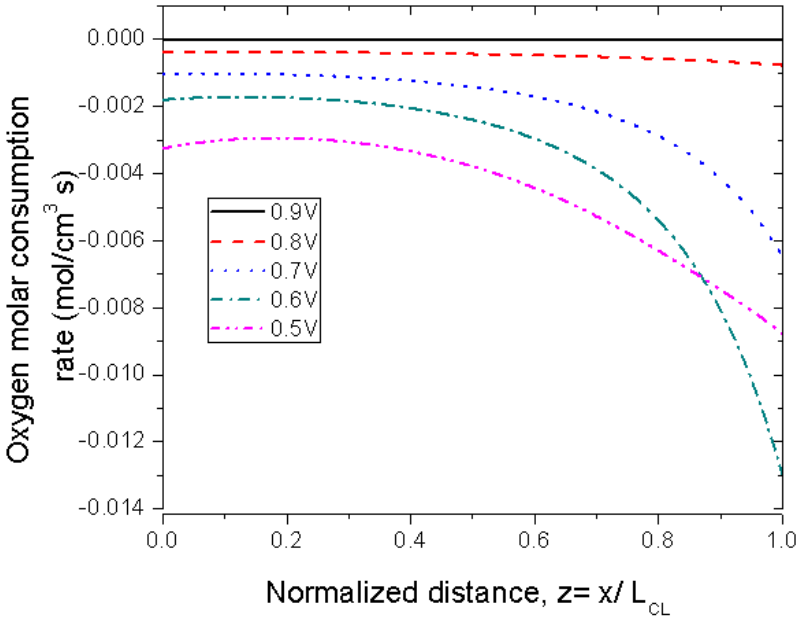

(b)

Figure 7 (a) Overall effectiveness-factor profile and (b) oxygen molar-consumption rate at different cell potentials across the catalyst layer.

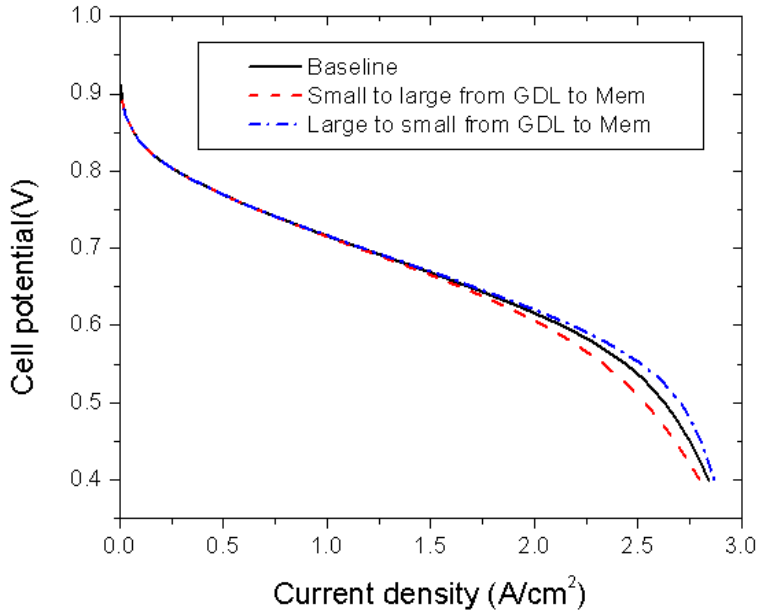

(a)

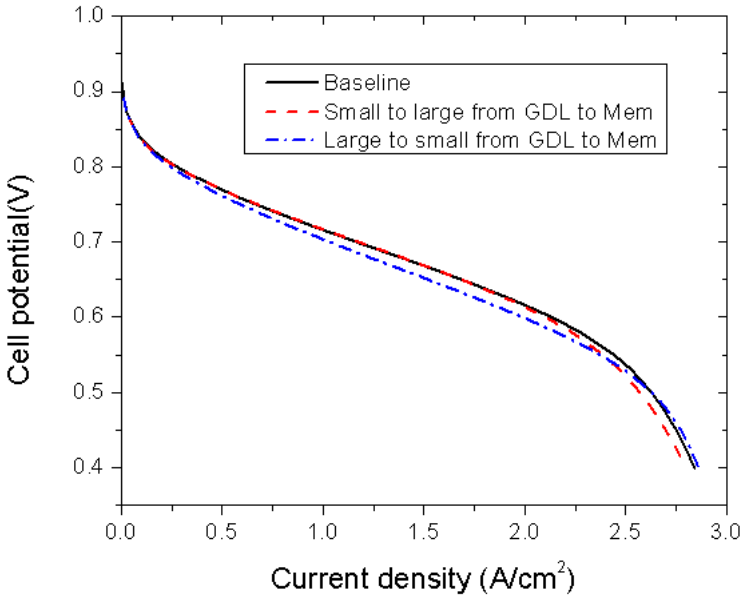

(b)

Figure 8 (a) Comparison of polarization curves for the cases of three different particle distributions when the film thickness varies proportionally and (b) when the film oxygen resistance is constant, $R_{O_2,film}$ = 0.01 m^2 s bar/mol.

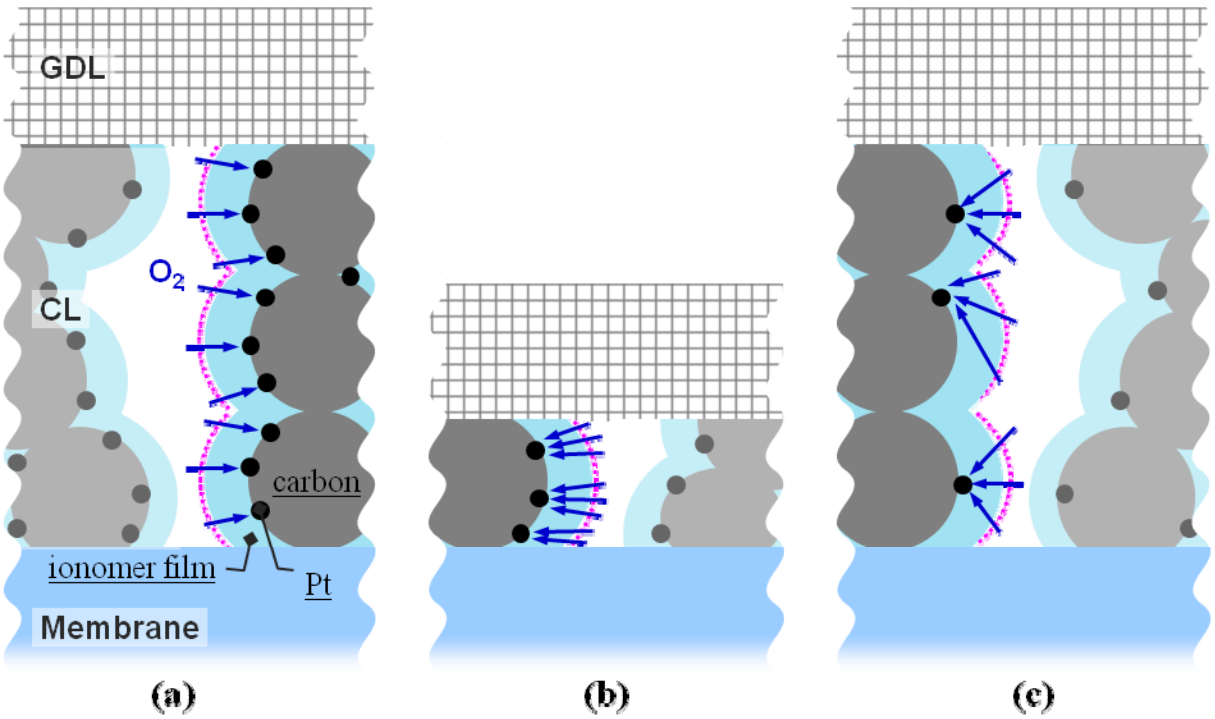

Figure 9 Schematic image of oxygen transport through the ionomer film for (a) normal CL structure and two low Pt-loading cases, (b) thinner CL, and (c) low Pt/C ratio. Figure adopted from reference 32.

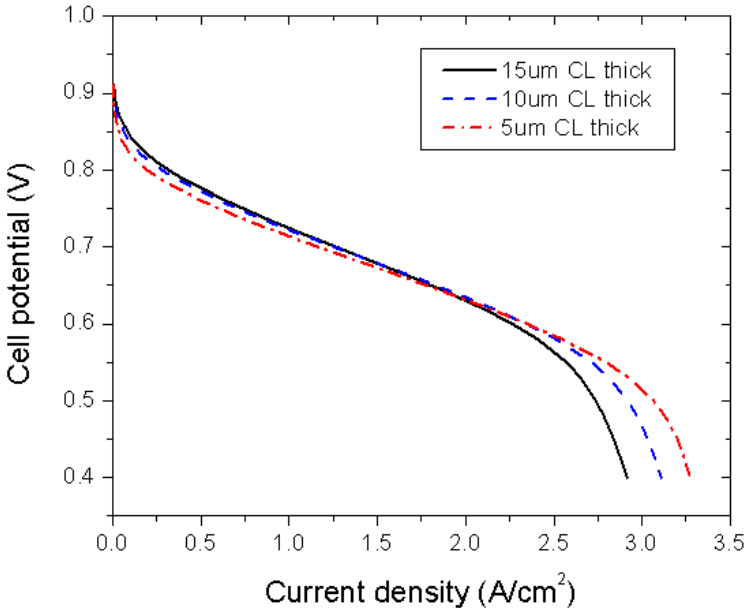

(a)

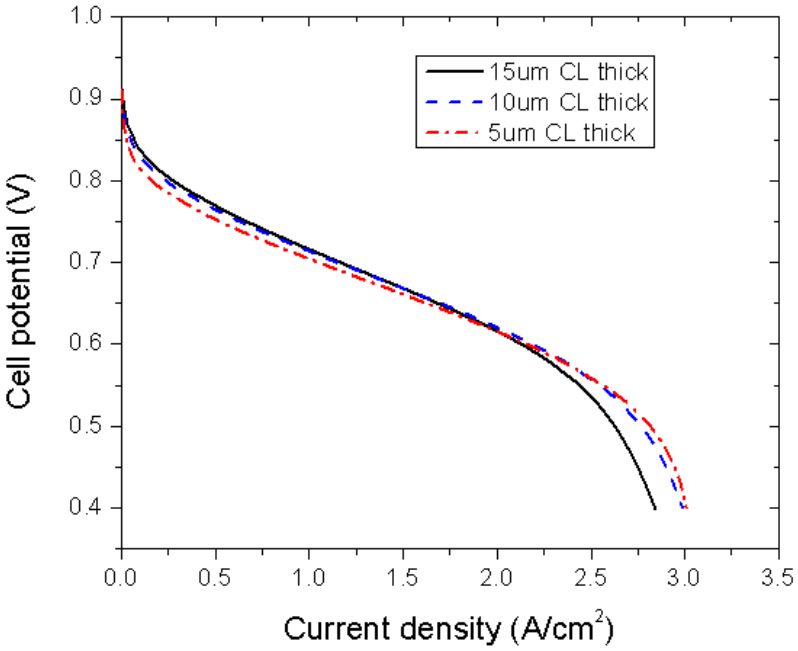

(b)

Figure 10 Polarization curves without (a) and with (b) ionomer film for three different CL thicknesses, $R_{O_2,film}$ = 0.01 m^2 s bar/mol.

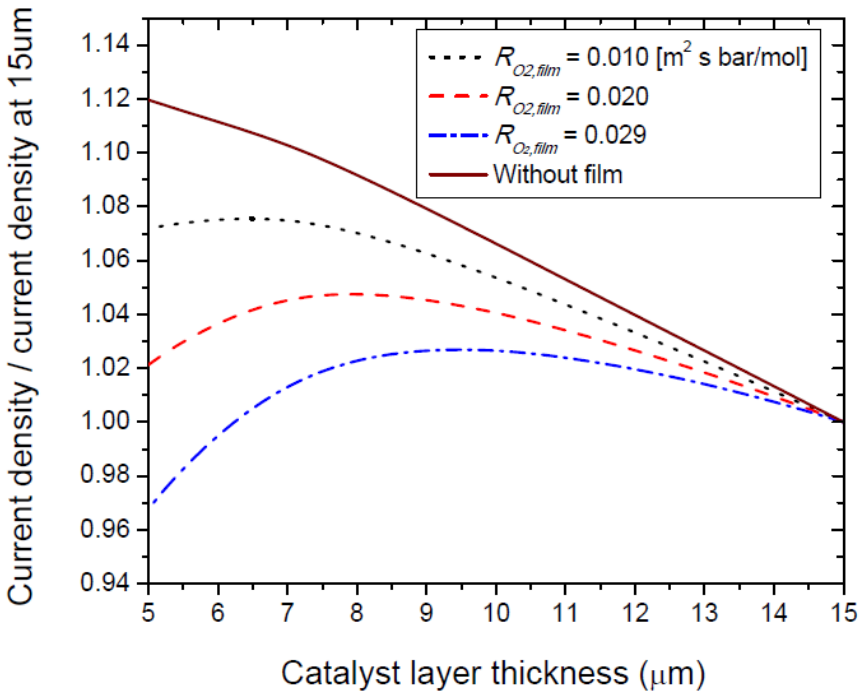
Current density / current density at 15um
Catalyst layer thickness (μm)
$R_{O2,film}$ = 0.010 [m^2 s bar/mol]
$R_{O2,film}$ = 0.020
$R_{O2,film}$ = 0.029
Without film

(a)

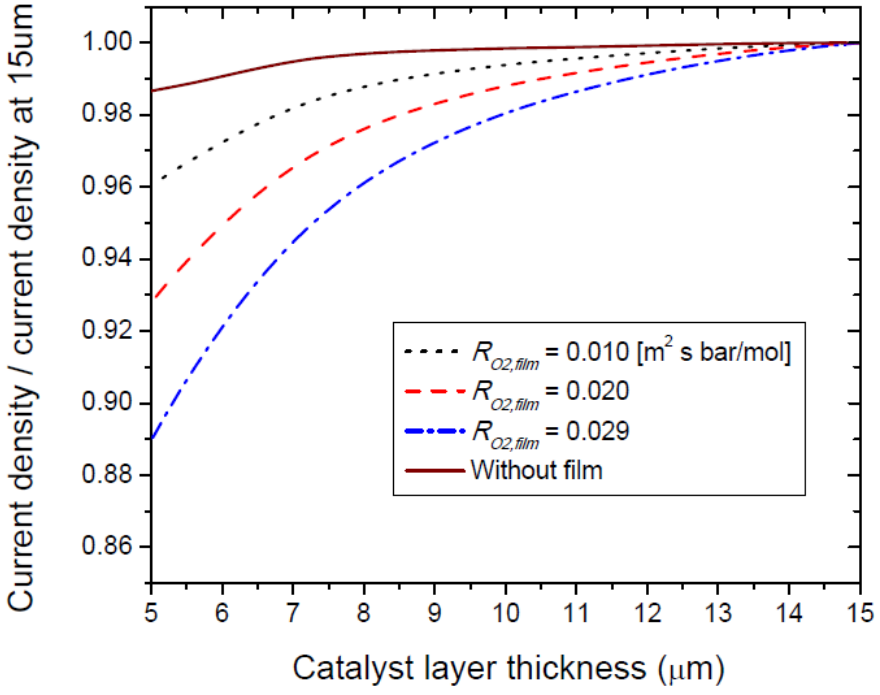
Current density / current density at 15um
Catalyst layer thickness (μm)
$R_{O2,film}$ = 0.010 [m^2 s bar/mol]
$R_{O2,film}$ = 0.020
$R_{O2,film}$ = 0.029
Without film

(b)

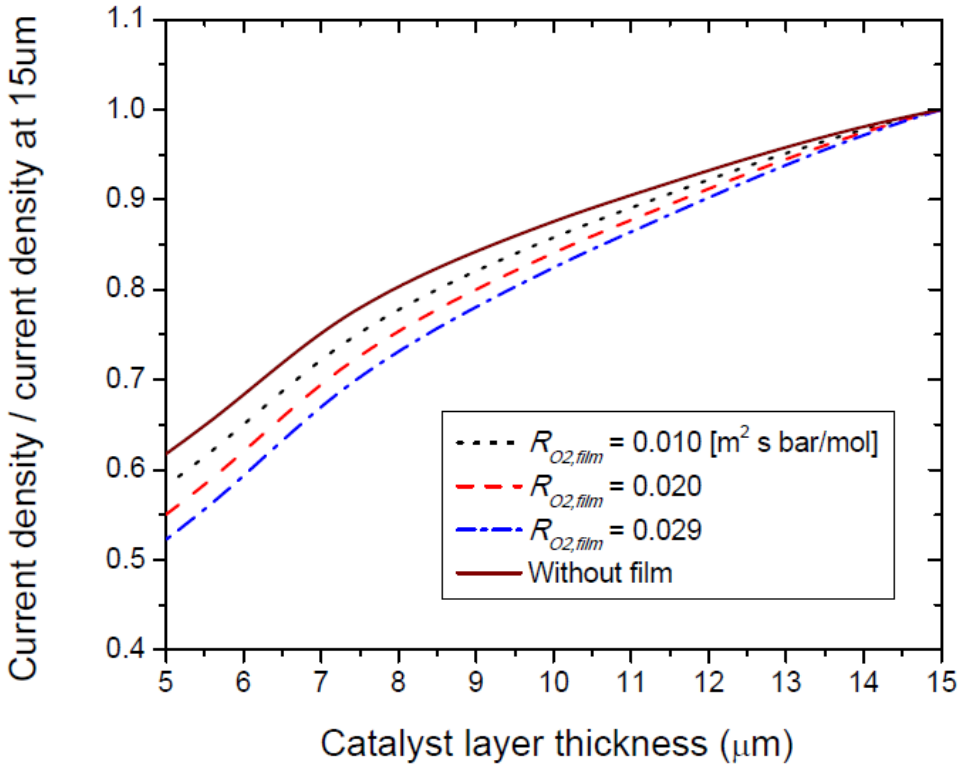

(c)

Figure 11 Current density at 0.5V with different film thicknesses with respect to the CL thickness (a) normal diffusion coefficients, (b) fast diffusion coefficients in the CLs, and (c) current density at 0.8V with different film thicknesses with respect to the CL thickness and normal diffusion coefficients

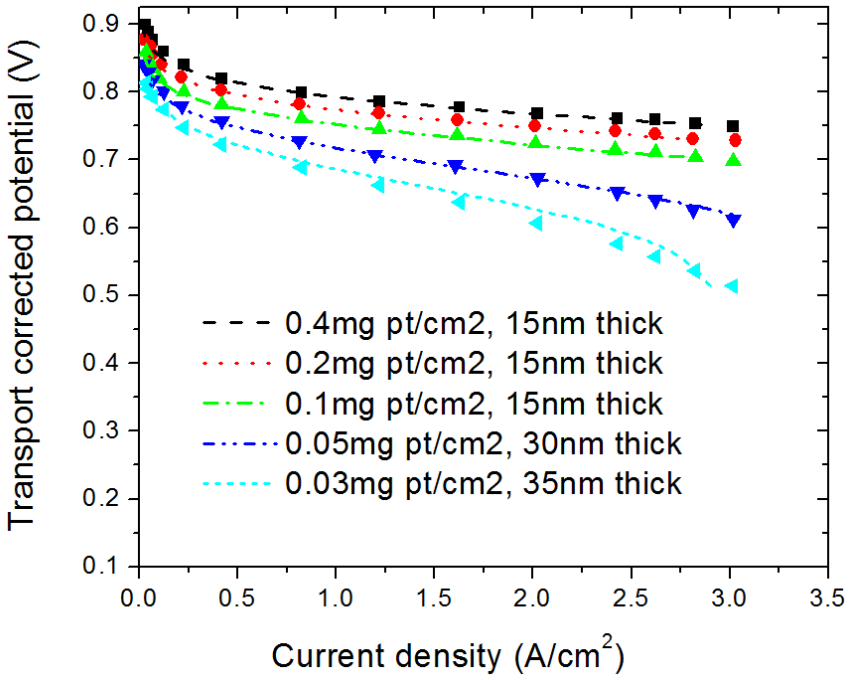

(a)

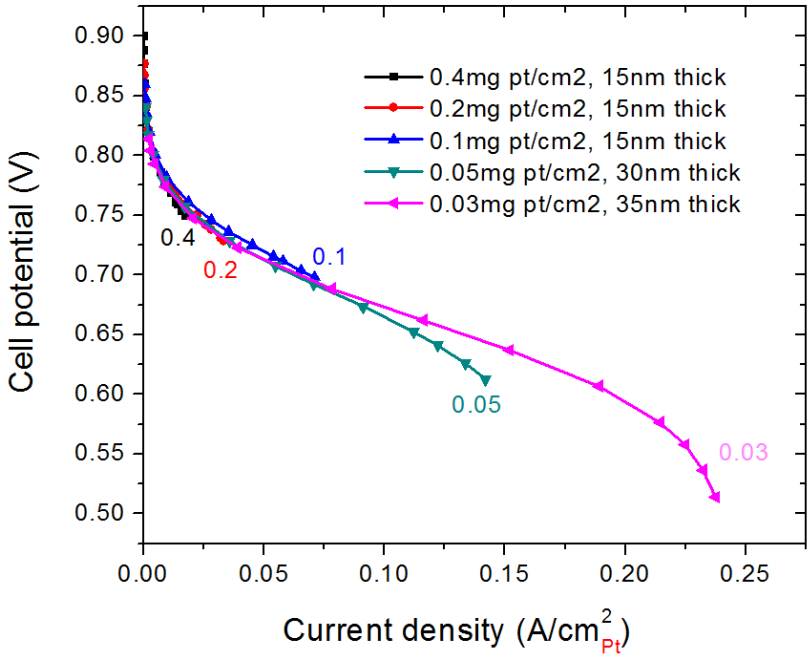

(b)

Figure 12 (a) Comparison of polarization curves with different Pt loadings between experimental data [61] (points) and model results and (b) simulated cell potential as a function of catalyst specific activity.

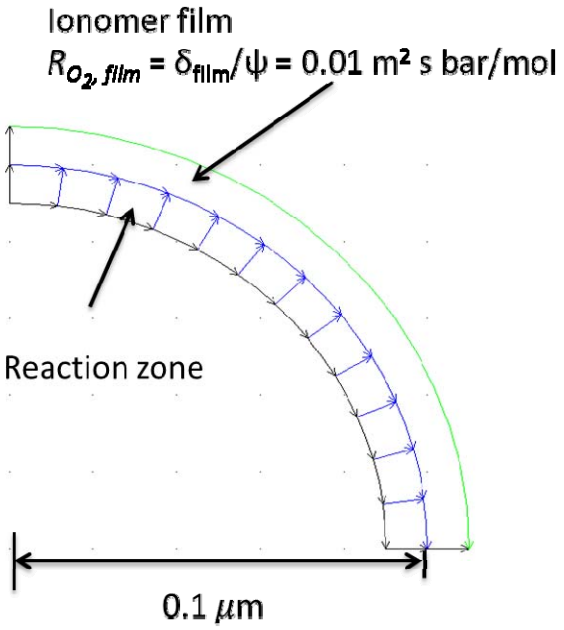
Ionomer film
$R_{O_2,\,film} = \delta_{film}/\psi = 0.01$ m² s bar/mol
Reaction zone
0.1 μm

(a)

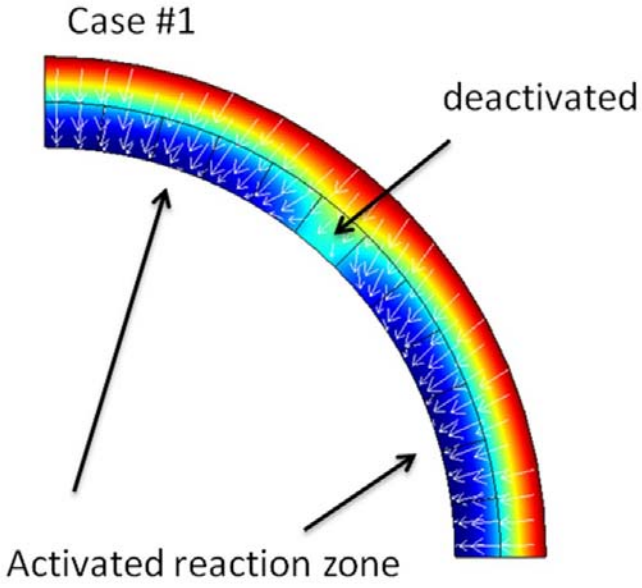
Case #1
deactivated
Activated reaction zone

(b)

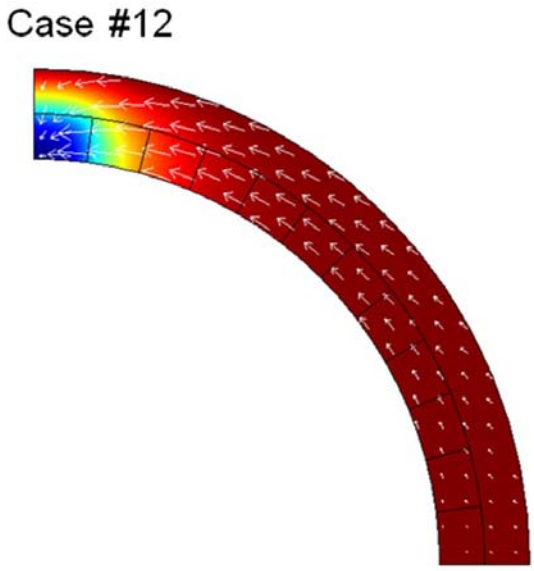

(c)

Figure 13 (a) Computational domain of two dimensional simplified agglomerate particle model, (b) a simulation result showing oxygen concentration and flux for case #1, and (c) at case #12. (Current density of 0.025A/cm^2 at the surface is given)

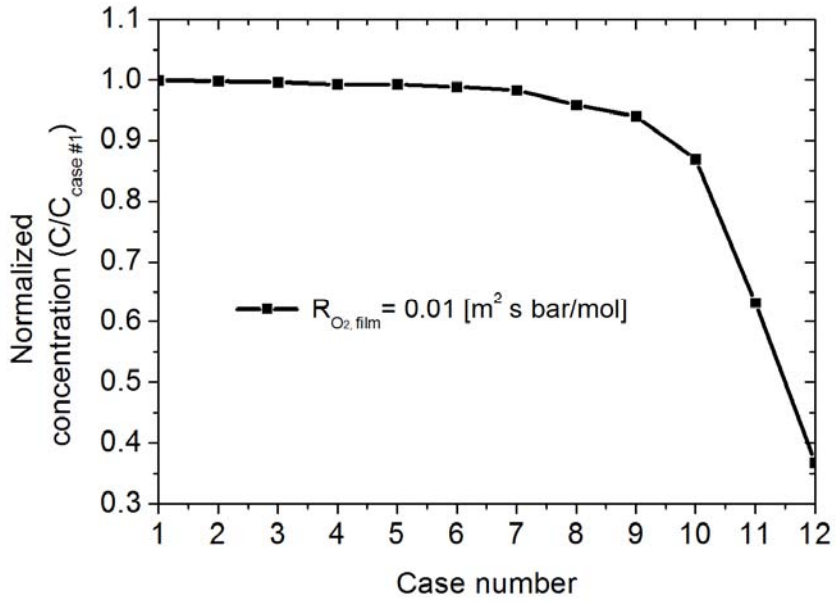

(a)

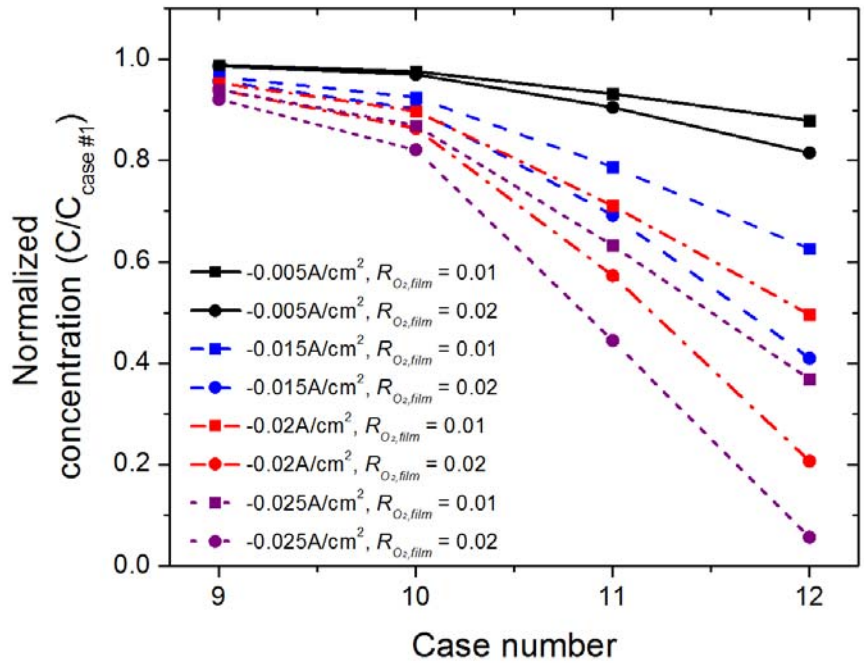

(b)

Figure 14 (a) Normalized oxygen concentration around the reaction zones and (b) concentration drop at case #9, 10, 11, and 12 with respect to agglomerate current density and two different film resistances.